Processing-dependent thermal stability of a prototypical amorphous metal oxide

Li Zeng,[1] Mahyar M. Moghadam,[2] D. Bruce Buchholz,[2] Ran Li,[2] Denis T. Keane,[2,3] Vinayak P. Dravid,[2] Robert P. H. Chang,[2] Peter W. Voorhees,[2] Tobin J. Marks,[1,2,4] and Michael J. Bedzyk[1,2,3,5,*]

[1]*Graduate Program in Applied Physics, Northwestern University, Evanston, Illinois 60208, USA*
[2]*Department of Materials Science and Engineering, Northwestern University, Evanston, Illinois 60208, USA*
[3]*Northwestern Synchrotron Research Center, Argonne, Illinois 60439, USA*
[4]*Department of Chemistry, Northwestern University, Evanston, Illinois 60208, USA*
[5]*Department of Physics and Astronomy, Northwestern University, Evanston, Illinois 60208, USA*

(Received 28 September 2017; published 15 May 2018)

Amorphous metal oxides (AMOs) are important candidate materials for fabricating next-generation thin-film transistors. While much attention has been directed toward the synthesis and electrical properties of AMOs, less is known about growth conditions that allow AMOs to retain their desirable amorphous state when subjected to high operating temperatures. Using *in situ* x-ray scattering and level-set simulations, we explore the time evolution of the crystallization process for a set of amorphous In_2O_3 thin films synthesized by pulsed-laser deposition at deposition temperatures (T_d) of −50, −25, and 0 °C. The films were annealed isothermally and the degree of crystallinity was determined by a quantitative analysis of the time-evolved x-ray scattering patterns. As expected, for films grown at the same T_d, an increase in the annealing temperature T_A led to a shorter delay prior to the onset of crystallization, and a faster crystallization rate. Moreover, when lowering the deposition temperature by 25 °C, a 40 °C increase in annealing temperature is needed to achieve the same time interval for the crystals to grow from 10 to 90% volume fraction of the sample. Films grown at $T_d = 0$ °C exhibited strong cubic texture after crystallization. A level-set method was employed to quantitatively model the texture that develops in the microstructures and to determine key parameters, such as the interface growth velocity, the nucleation density, and the activation energy. The differences observed in the crystallization processes are attributed to the changes in the atomic structure of the oxide and possible nanocrystalline inclusions that formed during the deposition of the amorphous phase.

DOI: 10.1103/PhysRevMaterials.2.053401

I. INTRODUCTION

Transparent conducting oxides (TCO) and transparent oxide semiconductors (TOS) are important candidate component materials for the next generation of thin-film transistors (TFTs) due to their excellent optical transparency, electrical mobility, and mechanical flexibility [1–4]. Recently, a preference for amorphous TCO and TOS (a-TCO/TOS) over their crystalline counterparts has emerged due to the following advantages [5–7]. Because of the lack of grain boundaries, a-TCO and a-TOS thin films possess higher film uniformity, smoother surfaces, and enhanced mechanical flexibility. The lower deposition temperatures ($T_d < 250$ °C) for a-TCO/TOS enables fabrication on flexible substrates, such as plastics [8–10]. Another advantage is the ability to maintain a relatively high mobility $\mu(\geqslant 10\,\mathrm{cm^2\,V^{-1}\,s^{-1}})$ while the structure is amorphous. Note that this is the opposite effect seen for the case of amorphous silicon (a-Si:H), where the mobility is ∼2 orders of magnitude lower than crystalline Si. The mobility of a-TCO/TOS is relatively insensitive to the structural disordering because the large nondirectional *n*s orbitals ($n \geqslant 4$) of transition-metal ions provide dispersive electron conduction paths [11]. Therefore, a-TCO/TOS present great potential and are attracting much attention for applications in TFT fabrication.

Typically, a-TCO/TOS are In_2O_3-based amorphous metal oxides (AMOs) with the introduction of metal ion dopants such as (Zn^{2+}, Sn^{4+}, Ga^{3+}, Y^{3+}, La^{3+}, etc.) [12–14], or organic species [15,16]. Amorphous indium-gallium-zinc oxide is one of the most widely used AMOs with its industrial applications as a semiconductor layer in TFTs [11,17,18]. Much research has been conducted to synthesize AMOs by methods such as sputtering, pulsed-layer deposition (PLD), and solution-processing [14]; to tune and optimize the electrical properties from either growth conditions or postgrowth treatments [19]; and to study the structure-property relations theoretically and experimentally [20–23]. In contrast, there are many fewer reported studies into the thermal stability of AMOs [24–29]. Temperature is a critical parameter in thin-film processing which allows for the fine-tuning of structure and properties. For example, when lowering substrate deposition temperature ($T_d < 0$ °C), various techniques such as dc magnetron sputtering and PLD can grow a-TCO/TOS [30–32]. Therefore an improved understanding of a-TCO/TOS when subjected to thermal treatments would be of great importance in terms of the cost, processing, and applications of these materials.

To exclude the effects and ambiguity introduced by dopants, this paper will concentrate on pure In_2O_3, since it is the key matrix material for a-TCO/TOS. In our prior research, a series of PLD-synthesized In_2O_3 thin films were grown with substrate temperatures T_d varying from −100 to 600 °C; as T_d increased, the degree of crystallinity increased in these as-deposited films [31]. Our earlier detailed *ab initio* molecular dynamics simulation and x-ray absorption fine-structure study of the as-deposited In_2O_3 films also indicated structural difference in

*Corresponding author: bedzyk@northwestern.edu

the amorphous phase, such as local nanocrystalline inclusions (~3 nm) and InO_x polyhedral preferences and distributions [30]. These differences buried in the amorphous material could potentially alter the energy barriers for initializing crystallization, and affect the overall crystallization kinetics. Herein, we designed and conducted a thermal stability study to compare the crystallization process for PLD-grown amorphous In_2O_3 films deposited at different values of T_d.

The amorphous-to-crystalline transition can be described by the degree of crystallinity χ_c, which characterizes the crystalline fraction of the material ($0 \leqslant \chi_c \leqslant 1$). χ_c is typically determined through x-ray diffraction (XRD), which quantitatively distinguishes both crystalline and amorphous phases within the material. In this paper, an *in situ* grazing incidence wide-angle scattering (GIWAXS) technique is used to track crystalline fraction evolvement under thermal annealing. The time-sequenced GIWAXS patterns are used to calculate χ_c as a function of annealing time t, which is subsequently used to fit a theoretical model. Moreover, the analysis of the final crystalline patterns provides information, such as domain size and preferred orientations, which can help trace back the fundamental difference between amorphous films.

An isothermal annealing condition is chosen for this set of experiments, since it allows for one variable: annealing time t. Isothermal crystallization traditionally can be described by the Johnson-Mehl-Avrami-Kolmogorov (JMAK) equation:

$$\chi_c = 1 - e^{-Kt^n}, \tag{1}$$

where n is the Avrami exponent, $K = K_0 \exp(-E_a/k_B T_A)$ is a temperature-dependent rate constant, E_a is the activation energy, k_B is the Boltzmann constant, and T_A is the annealing temperature, which is held constant [33,34]. The JMAK equation is generally more accurate in describing a bulk transformation with an isotropic growth rate than the thin-film case, but the average value of the Avrami exponent n can still be helpful in determining the growth dimensionality (*Dim*) and understanding the nucleation mechanism. The dimensionality (*Dim*) is 1, 2, or 3 for one-, two-, or three-dimensional growth, respectively. For the site-saturated nucleation (SSN) case, where nucleation only occurs at the beginning and no additional nucleation sites are formed during the growth, $n = Dim$. However, if there are new nuclei added to the system at a constant rate, known as the constant nucleate rate (CNR) case, $n = Dim + 1$ [35,36]. For thin-film crystallization, when the grain size is sufficiently small compared to film thickness, the crystallization can be considered as three-dimensional growth. In contrast, if the growing crystallites reach the film surface or film/substrate interface, the finite film thickness confines the crystallites to grow laterally, which leads to two-dimensional growth. In general, the average Avrami exponent n is expected to be $2 \leqslant n \leqslant 3$ for the SSN case ($n = Dim$), and $3 \leqslant n \leqslant 4$ for the CNR case. A more rigorous approach, namely the level-set method (LSM), is also employed in this paper. It is a numerical route used to track the time-dependent evolution of shapes and interfaces by providing for topological changes of nuclei growth and collisions, which also has the advantages of versatility and flexibility of modeling initial crystalline fraction, interface velocity, and object dimensions.

Herein, the isothermal crystallization of 300-nm In_2O_3 thin films grown on Si substrates at three temperatures T_d and annealed at three temperatures T_A are carefully studied and well characterized through *in situ* x-ray scattering techniques and level-set simulations. This provides an improved understanding for the thermal stability of In_2O_3 films, the fundamental thin-film crystallization, and ultimately the differences buried in the amorphous phase via the control of deposition temperature.

II. METHODS

A. Thin-film sample preparation

Amorphous In_2O_3 films with 300-nm thicknesses were grown on $10 \times 10 \times 0.4$-mm^3 Si substrates by PLD. A 248-nm KrF excimer laser with 25-ns pulse duration and operated at 2 Hz and a dense hot-pressed In_2O_3 target (25-mm diameter) were used for the PLD process. The 200-mJ/pulse beam was focused onto a 1-mm × 3-mm spot size. The target was rotated at 5 rpm about its axis to prevent localized heating. The target-substrate separation was fixed at 10 cm. The films were grown in an O_2 ambient of 8 mTorr. The substrates were attached to the substrate holder with silver paint. Three sets of films were grown under three deposition temperature (T_d): −50, −25, and 0 °C controlled by using liquid nitrogen [30].

B. *In situ* GIWAXS

In situ GIWAXS was employed to study the isothermal crystallization process of the In_2O_3 films. The experiment

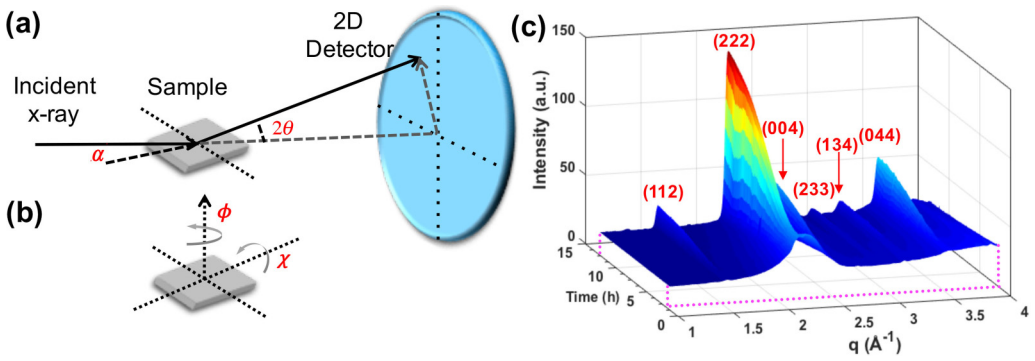

FIG. 1. (a) Schematic for GIWAXS setup with incident angle α. (b) Definition of the sample tilt angle χ and azimuthal angle ϕ. (c) Time sequence of 1D x-ray diffraction patterns from In_2O_3 film ($T_d = -25$ °C, $T_A = 180$ °C). The 0 to 2-h patterns (not shown) are essentially identical to the data at 2 h.

TABLE I. Summary of crystallization time τ_C, Avrami constant n, and postannealed domain size D.

Sample No.	T_d (°C)	T_A (°C)	τ_C (min)	n	D_{222} (nm)	D_{004} (nm)
1	−50	220	376	2.48	45.9	44.4
2	−50	230	79	3.85	45.7	39.3
3	−50	240	46	3.87	41.1	33.5
4	−25	180	678	2.56	45.2	47.9
5	−25	190	278	2.41	42.8	40.3
6	−25	200	132	2.60	45.5	43.3
7	0	120	1520	2.66	39.9	55.8
8	0	130	496	2.42	38.0	50.5
9	0	140	250	2.52	36.9	53.0

[Fig. 1(a)] was performed at the DuPont-Northwestern-Dow Collaborative Assess Team (DND-CAT) 5BM-C station at the Advanced Photon Source (APS) using a 20.00-keV x-ray beam with a 20-μm by 400-μm incident beam size and $\sim 10^7$ photons/s flux. The incidence angle was fixed at $\alpha = 0.17^\circ$, which is slightly greater than the critical angle of $\alpha_c = 0.14^\circ$ for In_2O_3 at this energy. This caused an x-ray penetration depth of ~200 nm and ensured that only the film would be probed by the incident x-ray beam. The samples were annealed under vacuum condition ($\sim 2 \times 10^{-7}$ bar) controlled in a minichamber with a beryllium dome mounted on the diffractometer, with a pyrolytic boron nitride-coated pyrolytic graphite heating stage. The sample temperature was monitored with a thermocouple in contact with the film surface. For a set of In_2O_3 films deposited at the same T_d, each was annealed isothermally at a fixed annealing temperature T_A. For example, the three films deposited at $T_d = -25\,^\circ$C were annealed at 180, 190, and 200 °C, respectively. In total, nine crystallization transitions, summarized in Table I, were measured and studied to estimate the effects of initial growth conditions. A Mar165 charge-coupled device (2048 by 2048 pixels; pixel size 79 by 79 μm) area detector was placed ~180 mm away from the sample to collect a 100-s exposure-time GIWAXS diffraction pattern in 120-s time intervals. The 2D area detector was calibrated by XRD from a lanthanum hexaboride (LaB_6) standard powder sample. An x-ray shutter-closed dark image was recorded for background subtraction.

The NIKA package was used for 2D image data reduction [37]. The beam center position, sample-to-detector distance L, and detector tilting angles were refined from the calibration of the LaB_6 standard. These refined parameters were then used as input parameters to convert experimental 2D images into intensity data as a function of momentum transfer $q = 4\pi \sin\theta/\lambda$. A 1D profile [$I(q)$ vs q] was generated by circularly averaging the diffraction rings on the 2D images. The degree of crystallinity χ_c for each diffraction pattern is calculated through the Ruland method [38,39]:

$$\chi_c = \frac{\int_0^\infty q^2 I_c(q) dq}{\int_0^\infty q^2 I(q) dq}, \tag{2}$$

where the numerator is the summed-up net areas under all the crystalline diffraction peaks [$I_c(q)$] and the denominator is the integrated intensity under the entire scattering pattern [$I(q)$]. Equation (2) underestimates the crystalline fraction because $I_c(q)$ does not include diffuse scattering due to thermally induced atomic vibrations and lattice imperfections. How this is corrected with a Debye-Waller factor is included in Sec. S1 of the Supplemental Material along with a detailed description of the χ_c analysis [40].

The domain size D_{hkl} in certain (hkl) directions at the final crystalline phase ($\chi_c \to 1$) is determined by applying the Scherrer formula to the peak width ($D_{hkl} = 1.8\pi/\Delta q$) [41]. See Sec. S2 of the Supplemental Material for detailed geometrical corrections applied to peak width [40]. The width of two diffraction peaks, (222) and (004), are analyzed in the paper, and the experimental data are fitted to a Voigt function. In summary, for each crystallization process, the degree of crystallinity χ_c as a function of annealing time t, and the crystallite size D of the after-annealed crystalline film were determined by GIWAXS analysis and will be compared to a level-set simulation described below.

C. Texture analysis

The distribution of grain orientation for selected films was studied locally by electron backscatter diffraction (EBSD) and over a macroscopic volume by x-ray pole figure (PF) measurements. The EBSD maps were taken on an FEI Quanta ESEM at 20 keV using a 300-nm step size. OXFORD AZTEC EBSD software was used for data reduction. The x-ray PF measurements, which were performed at APS 33BM-C, are similar to the Schulz reflection method [41], but use an area detector (Pilatus 100K) to collect the pole figures [42,43]. With the incident angle α and diffraction angle 2θ fixed, diffraction patterns were collected as a function of tilt angle χ from 0 to 90° and azimuthal angle ϕ from 0 to 360°.

D. Level-set method simulation

The LSM is a powerful simulation scheme for moving boundary problems that can capture the evolution of complex interfacial topology [44,45]. The inherent geometrical nature of this method makes it an ideal approach for studying interface-controlled kinetic phenomena such as crystallization from the amorphous state or relaxation of polarized domains in ferroelectrics [46]. The major distinction of this method from other simulation methodologies is its ability to evaluate and follow interfacial evolution on experimental length and time scales, which provides a unique opportunity for directly comparing simulation results with experimental measurements. In this approach, for a single grain, the level-set function is defined as a continuous signed distance function $\Phi(x,t)$, where the interface between crystal grain and amorphous is implicitly given by $\Phi(x,t) = 0$. It evolves through the equation of motion as:

$$\frac{\partial \Phi}{\partial t} + \boldsymbol{V} \cdot \nabla \Phi = 0, \tag{3}$$

where $\boldsymbol{V}$ is the velocity of the amorphous-crystal interface. Equation (3) is numerically solved using a forward Euler time-discretization scheme in 3D Cartesian coordinates. In isotropic growth, the interface velocity ($\boldsymbol{V}$) is independent of the normal to the interface, which results in spherical domains. In the anisotropic case, the interface velocity is a function of different parameters like curvature, orientation, concentration, and temperature. Previous studies on indium-oxide systems

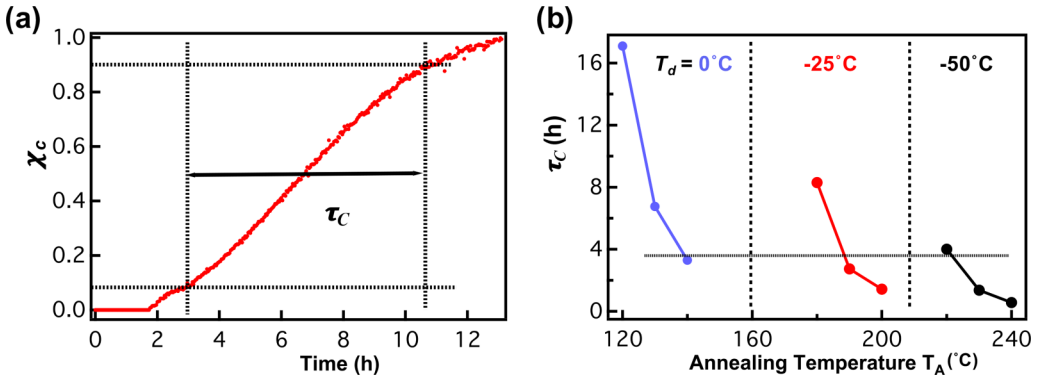

FIG. 2. (a) Based on Eq. (2), experimentally determined degree of crystallinity (χ_c) as a function of annealing time. This example is for the film deposited at $T_d = -25\,^\circ$C and held at $T_A = 180\,^\circ$C. All nine crystallization curves are shown in Fig. 5. Crystallization time τ_C is defined as the time interval between $\chi_c = 0.1$ and $\chi_c = 0.9$. (b) Crystallization time as a function of annealing temperature T_A for the three films deposited at each T_d (0, −25, and −50 °C).

have shown fully faceted cubic crystal growth during crystallization [36,47–49]. Hence, in this work, we assume that $\boldsymbol{V}$ depends only on the crystallographic orientation of the faceted interface. Therefore, the velocity at a point on the interface is $\boldsymbol{V} = \gamma(\boldsymbol{n})\boldsymbol{n}$, where $\boldsymbol{n}$ is an interface normal at a given point and Eq. (3) changes to its new format as follows:

$$\frac{\partial \Phi}{\partial t} + \gamma(\boldsymbol{n})\boldsymbol{n} \cdot |\nabla \Phi| = 0. \tag{4}$$

To determine $\gamma(\boldsymbol{n})$, we employ Russo-Smereka's approach [50] for faceted growth, which has been proven to deliver correct kinetic Wulff shapes for a given morphology. In this approach $\gamma(\boldsymbol{n})$ is defined as shown in Eq. (5):

$$\gamma(n) = v_F + u\sqrt{1 - (\boldsymbol{n} \cdot \boldsymbol{n}_F)^2}. \tag{5}$$

Here, v_F and u are facet normal and tangential velocity and $\boldsymbol{n}_F$ denotes the facet normal direction. Equation (5) enforces that the normal to every point on the interface is in a facet orientation. For instance, in cubic growth, the surface normal adopts one of the six ⟨100⟩ directions of the facets. The tangential term ensures edges where two facets meet and thus ensures fully faceted evolution of the grain. The detailed implementation of Russo-Smereka's approach and its integration into our LSM algorithm for simulation of the growth of faceted crystals is discussed in a previous study [49].

III. RESULTS

A. Crystallization process

The thermally induced structural evolution was monitored by GIWAXS. Indium oxide has the bixbyite structure (space group $Ia\bar{3}$, ICSD No. 169420, Fig. S1 in the Supplemental Material) with the lattice constant $a = 10.117$ Å [40]. A simulated 1D diffraction pattern is included in Fig. S2 in the Supplemental Material [40]. A time sequence of 1D diffraction patterns from an In_2O_3 film that was deposited at $T_d = -25\,^\circ$C and held at $T_A = 180\,^\circ$C is presented in Fig. 1(c). For the first ∼2 h the patterns exhibit two broad amorphous scattering peaks, after which In_2O_3 diffraction peaks grow in time with the reduction of the amorphous peaks. After ∼12 h, the amorphous-to-crystalline transition approaches completion and sharp diffraction peaks indicate the formation of large crystalline domains. Using Ruland's method [Eq. (2)], the degree of crystallinity $\chi_c(t)$ as a function of annealing time t is extracted from the data and is presented in Fig. 2(a). This crystallization process curve demonstrates the typical "S" shape with three regions: the beginning region is related to a long incubation time for initial nuclei to precipitate and overcome the activation energy; followed by a middle region with a steep slope where fast crystallization and crystallite growth occur; and finally, as the crystalline grains expand and meet at the grain boundaries, the film slowly approaches full crystallinity. Similar analyses were carried out to generate crystallization curves for each T_d,T_A combination.

Before introducing a quantitative model-dependent simulation to interpret the evolution of the degree of crystallinity, a simple approximation of the crystallization time τ_C is computed by the time elapsed from 10% crystallinity until crystallization reaches 90% crystallinity as shown in Fig. 2(a). The extracted crystallization time τ_C for all nine samples is plotted in Fig. 2(b). As expected from Eq. (1) for films deposited at the same T_d, lowering the annealing temperature T_A requires a longer annealing time τ_C. Lower T_A leads to a slower grain growth rate and nuclei formation rate, which results in a longer annealing time. Another way to interpret Fig. 2(b) is to estimate the required annealing temperature if all films crystalize within the same time. For example, if three films deposited at $T_d = 0$, −25, and −50 °C are expected to have the same $\tau_C \sim 4$ h, the annealing temperature T_A would be ∼135, 180, and 220 °C, respectively. There is an approximately 40 °C increase in T_A as T_d decreases by 25 °C. Therefore, even though as-deposited films are amorphous, there are intrinsic structural differences resulting from the deposition temperature T_d which affect the subsequent crystallization.

Our previous results for 60- and 300-nm In_2O_3 films deposited on quartz substrates can shed light on this phenomenon [30,31]. (There was no postannealing in these previous studies.) With the decrease of deposition temperature ranging from 600 to −100 °C, the degree of crystallinity decreased for the 300-nm film, and stayed at its amorphous phase for T_d below 0 °C. Nanocrystalline inclusions were observed for amorphous In_2O_3 ($T_d \leqslant 0\,^\circ$C) and the size of the nanocrystalline inclusions trended to be larger for higher T_d. A similar

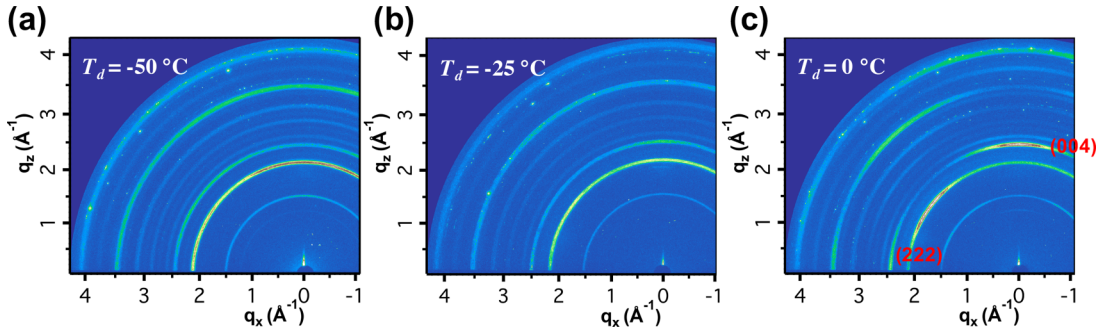

FIG. 3. 2D GIWAXS patterns of after-annealed crystalline In_2O_3 thin films deposited at $T_d = -50\,^{\circ}C$ (a), $-25\,^{\circ}C$ (b), and $0\,^{\circ}C$ (c).

crystallinity trend was shown for the 60-nm films. Moreover, lower deposition temperature reduced the film density as determined by x-ray reflectivity measurements. Hence, for films deposited at higher T_d, the as-deposited amorphous In_2O_3 film should have more relaxed lattice structures, and possibly more/larger nanocrystalline inclusions compared to lower T_d films. These nanosized crystalline-phase In_2O_3 inclusions are considered to serve as the initial crystallization nuclei, and the more relaxed structures will have a lower energy barrier for crystalline phases to grow, which promotes the crystallization velocity, and a much lower annealing temperature is required.

B. Texture analysis of postannealed fully crystalline films

The time-sequenced collection of the crystalline GIWAXS patterns [Fig. 1(c)] also provides information about the preferred crystallite orientation, i.e., thin-film texture, from which the crystallite growth directions can be traced. GIWAXS patterns with uniform Bragg diffraction rings, such as shown in Figs. 3(a) and 3(b), correspond to polycrystalline films without preferred orientation, whereas Fig. 3(c) is from a textured polycrystalline film and hence shows nonuniform rings. For all nine cases, strong texturing occurred for the three films deposited at the highest temperature of $T_d = 0\,^{\circ}C$ (Fig. S4 in the Supplemental Material) [40].

The [001] pole density shown in Fig. 4(a) (bottom) of the $T_d = 0\,^{\circ}C$, $T_A = 130\,^{\circ}C$ fully crystalline film was collected at the 2θ for the (004) Bragg condition in reflection geometry (i.e., at $\alpha = \beta = (2\theta)/2$, where α and β are the incident and scattered directions relative to the surface, respectively). The concentrated pole density in the center, at tilt angle $\chi = 0$, indicates that the crystallites have a preferred direction that aligns cubic unit-cell axes along the surface-normal direction of the film. The outer uniform ring at $\chi = 90^{\circ}$ corresponds to the other unit-cell axial directions lying in-plane with no preferred azimuthal ϕ orientation. Because the (222) Bragg ring lies close to the (004), as seen in Fig. 3(c), the collection of the 004 PF also allowed for simultaneous collection of the (222) PF as displayed in Fig. 4(a) (top). The uniform azimuthal density of the [222] poles at $\chi = 54.7^{\circ}$ is consistent with a cubic film having cube texture. This is also confirmed by the PF results from EBSD [Fig. 4(b)]. An example of a nontextured polycrystalline PF from an EBSD measurement is shown in Fig. S5 in the Supplemental Material for comparison [40]. A line-cut profile extracted from the x-ray (004) PF image of Fig. 4(a) (bottom) is shown in Fig. 4(c). This quantitatively describes the orientation distribution of the crystallite (004) poles about the surface-normal direction as having a width of 23°. This information will be used below in the LSM simulation as predefined nuclei-orientation input.

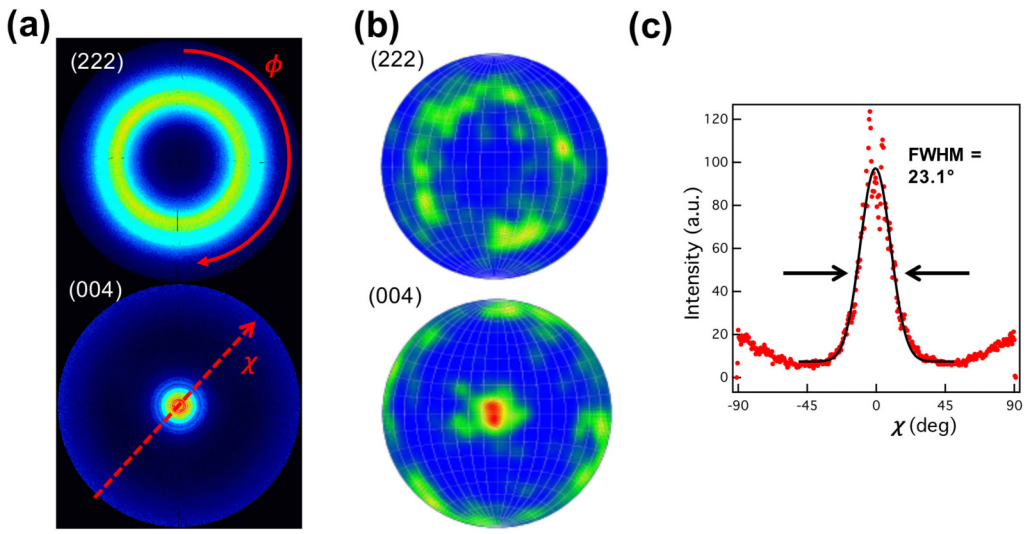

FIG. 4. PF from both x-ray (a) and EBSD (b) measurements of the crystalline In_2O_3 thin film ($T_d = 0\,^{\circ}C$, $T_A = 130\,^{\circ}C$) at (222) (upper) and (004) (lower) Bragg conditions. (c) The line-cut profile from x-ray PF (a, lower, dashed line path) with its Gaussian fit yielding a FWHM $= 23.1^{\circ}$.

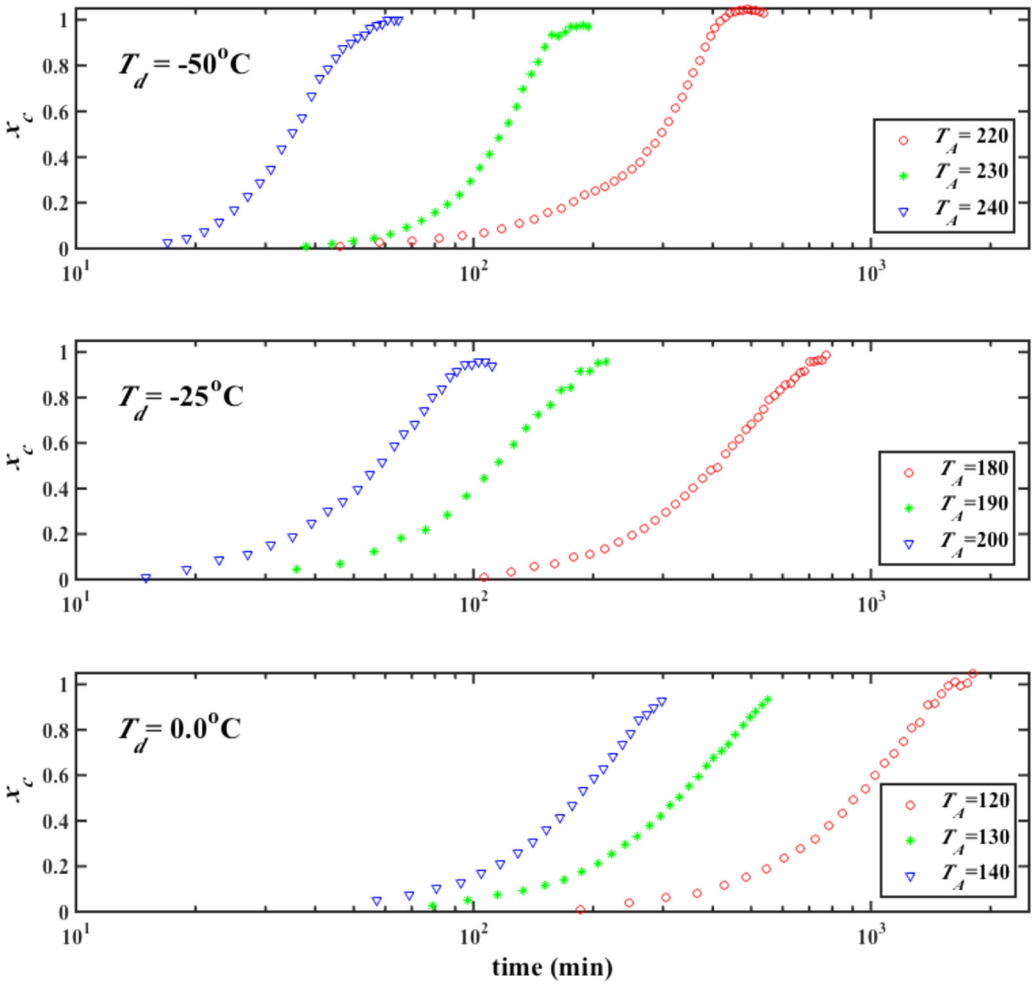

FIG. 5. The evolution of the degree of crystallinity of In_2O_3 films. For film deposited at the same T_d, three annealing temperatures (T_A) are shown.

This observed texturing suggests that films grown at a sufficiently high temperature (0 °C) may have nanocrystalline In_2O_3 inclusions within an amorphous matrix that have cube texture, whereas, within the amorphous films grown at lower T_d (−25 and −50 °C), the nanocrystalline inclusions could be nontextured. Therefore, in addition to the above effects of T_d shown on the crystallization time τ_C, the higher T_d leads to a lower energy barrier for the nanoscale crystallites to align with their preferred orientations [51].

C. Domain-size analysis of the fully crystalline films

The domain sizes D_{hkl} of the after-annealed crystalline films are extracted from the (222) and (004) diffraction peak widths and presented in Table I. For films deposited at $T_d = -25$ and -50 °C, $D_{222} \approx D_{004}$; while for the films deposited at $T_d = 0$ °C, the domain sizes along the two directions are different ($D_{004} > 50$ nm, $D_{222} < 40$ nm). This is consistent with the texturing analysis. For the textured film, the initial nanocrystalline inclusions align their (004) lattice planes perpendicular to the surface-normal direction; the growth of crystallites along the surface normal direction is less likely to be interrupted by their neighboring ones, and result in a longer length.

Electron microscopy images of the surface and grain morphology of the crystalline film ($T_d = 0$ °C and $T_A = 130$ °C) are shown in Fig. S6 in the Supplemental Material [40]. Note that even though some of the domains in the SEM image showed ∼μm size dimensions, they are not necessarily single-crystal domains. Therefore, the ensemble-averaged domain size derived from x-ray analysis is still valid.

D. Kinetics simulation and analysis

The temporal evolution of the crystallization process for different film deposition temperatures (T_d) at different annealing temperatures (T_A) is shown in Fig. 5. As expected, for each deposition temperature, with increasing annealing temperature the incubation time, i.e., the start of the transformation, decreases and the system undergoes faster crystallization, in agreement with the qualitative analysis in Fig. 2(b).

The first step to simulate the kinetics of crystallization via the level-set method is to identify the nucleation mechanism in the crystallization process, which can be done by calculating the Avrami exponent (n) from the crystallinity (χ_c) vs time (t) data. The Avrami exponent (n) can be determined by rearranging Eq. (1) as follows:

$$\ln[-\ln(1-\chi_c)] = \ln(K) + n\ln(t). \quad (6)$$

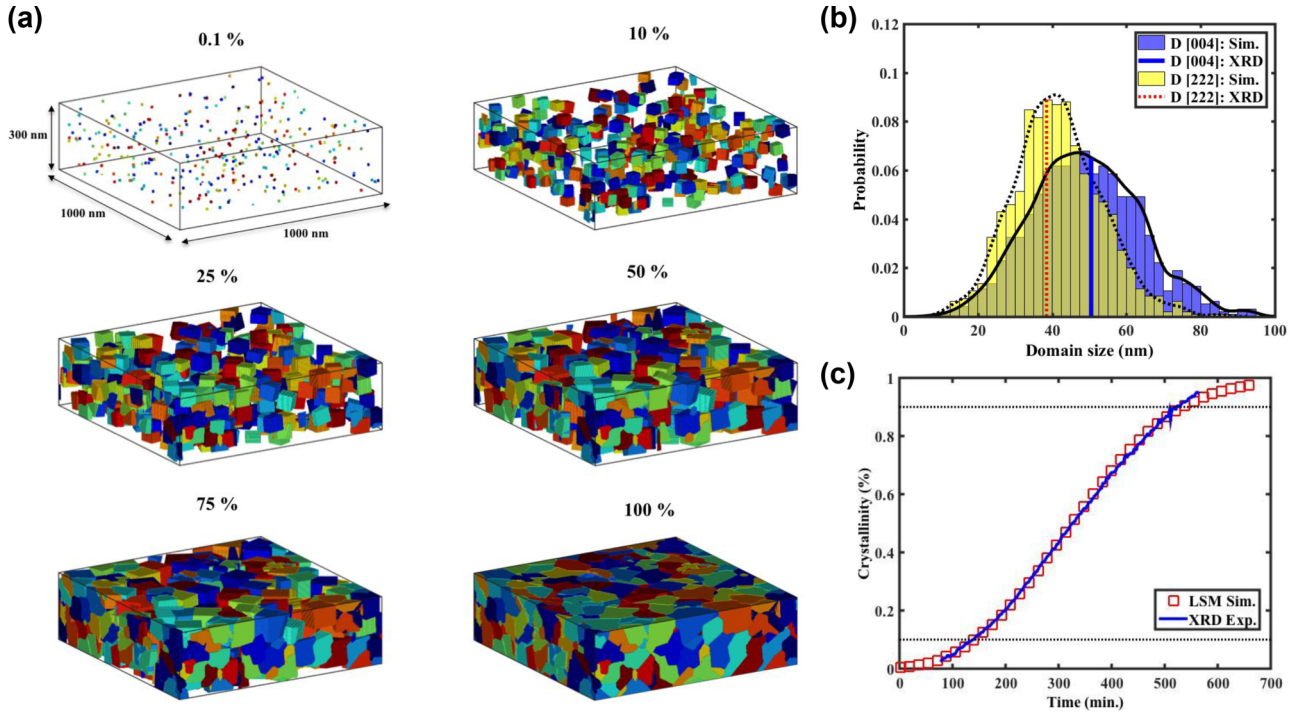

FIG. 6. Simulation results: (a) visualization of crystallization process modeled by the level-set method for site-saturated nucleation and faceted growth with only interfaces along the ⟨100⟩ directions. The transformed volume is shown. (b) Probability distribution of domain sizes along (004) and (222) plane directions. (c) Experimental and simulated crystallinity vs time plot, used to extract the interface velocity. The colors are chosen to visualize the individual grains.

The slope of the linear region in the Avrami plot ($\ln[-\ln(1-\chi_c)]$vs $\ln(t)$), shows the average value of the Avrami exponent (n). Avrami exponents for all samples have been summarized in Table I along with domain-size information and crystallization time (τ_C). Even though the governing assumption of the JMAK equation (bulk transformation with isotropic growth) is not entirely met in thin-film crystallization, previous studies show that the average value of the Avrami exponent n can still be used to determine the most probable nucleation mechanism [49]. Based on the relation between the Avrami exponent n and growth dimensionality (Dim), results in Table I suggest that, except for samples 2 and 3, the samples have values of n between 2 and 3, and have undergone crystallization through bulk site-saturated nucleation. During SSN all the crystal nuclei appear at the same time, and no further nucleation occurs at later times. The larger Avrami exponents n observed for samples 2 and 3 likely suggest continuous nucleation during crystallization.

Taking the above-discussed crystallization mechanism into account, sample 8 ($T_d = 0\,^\circ$C; $T_A = 130\,^\circ$C) is chosen for the detailed simulation of the transformation via the LSM method to account for the development of texture that is extracted from the PF measurement. In the simulation box, the XY plane is $1000 \times 1000\,\text{nm}^2$ and the Z direction is fixed at 300 nm. Periodic boundary conditions are imposed only on film lateral directions (both X and Y directions) to avoid size effects. The Z direction is along the film normal with a length equal to the film thickness. Since the nucleation mechanism for sample 8 is a site-saturated case, simulation starts with a fixed number of nuclei at the beginning of the crystallization. The orientation of each nucleus is assigned based on χ and ϕ angles [Fig. 1(b)], to resemble the texture structure observed in Fig. 4. The tilting angle (χ) with respect to [001] is taken from a Gaussian distribution (FWHM $= 23.1^\circ$) and the rotation angle (ϕ) around the [001] direction is randomly assigned between 0 and 360°. By changing the nucleation density (N_V) as a fitting parameter, it is found that setting $N_V = 1.07 \times 10^{-6}\,\text{nm}^{-3}$ generates the closest microstructure to the sample 8 case. To acquire statistically sufficient microstructure data, the simulation results are averaged over 20 runs with randomized initial configurations of the nuclei. Figure 6(b) shows simulation results for probability distribution density of the domain size D along the (004) and (222) plane-normal directions. The comparative results for domain sizes from XRD measurements and LSM simulation are summarized in Table II.

The above reasonable prediction of microstructures allows us to match the dimensionless time in the simulation to the crystallization time τ_C (Table I), and to determine the {001} interface facet velocity (v_F). For sample 8, it yields $v_F = 0.11\,(\text{nm/min})$. To determine interface velocity for films with the same T_d but annealed at other temperatures, similar simulations are performed on samples 7 and 9 with the same

TABLE II. Comparison of crystal domain sizes along [001] and [111] directions derived from (004) and (222) GIWAXS peaks and from LSM.

Domain size (nm)	[001]	[111]
GIWAXS peak widths	50.5	38.0
LSM simulation	50.	42.

assumption on the sample texture. The results yield facet velocities of 0.04 and 0.21 (nm/min), respectively. The temperature dependence of these values is then used to determine the activation energy of growth via an Arrhenius relation [36]. The activation energy is found to be −0.5 eV, which suggests that the crystallization process only includes the growth of nuclei. The data shown in Table I imply that there is no significant change in domain size for samples deposited at $T_d = 0\,^{\circ}\mathrm{C}$, which indicates relatively similar nucleation densities at different annealing temperatures. These simulation results performed for samples 7 and 9 confirm the SSN mechanism. This is also consistent with the hypothesis that nanocrystalline domains exist in the as-deposited films. The formation of nanocrystals can be seen at lower deposition temperatures as well. At relatively higher annealing temperatures (samples 2 and 3), it is possible that thermal energy is sufficient to overcome the energy barrier of homogeneous nucleation and to initiate nucleation with a constant rate during the crystallization process. This observation is in a good agreement with the higher values of the Avrami exponent n for samples 2 and 3, as well as a reduction in domain size for the $T_d = -50\,^{\circ}\mathrm{C}$ samples, which is also consistent with an increase in the number of nuclei with temperature.

IV. CONCLUSIONS

In situ GIWAXS measurements and level-set simulation were carried out to characterize the isothermal crystallization processes of PLD-deposited In_2O_3 thin films. Three sets of In_2O_3 films with the same thickness but different deposition temperatures T_d (−50, −25, 0 °C) were prepared and each set was investigated under three annealing temperatures T_A. The real-space structural evolution was monitored and recorded by 2D diffraction patterns, from which the degree of crystallinity χ_c as a function of annealing time t was extracted and calculated. As expected, for films grown at the same T_d, an increase in the annealing temperature T_A led to a shorter delay prior to the onset of crystallization, and a faster crystallization rate. Moreover, when lowering the deposition temperature by 25 °C, there is a 40 °C increase in annealing temperature to achieve the same time interval for the crystals to grow from 10 to 90% volume fraction of the sample.. The 2D diffraction patterns of the after-annealed crystalline films showed cubic texturing features for films deposited at 0 °C. Pole figures from both EBSD and x-ray measurements confirmed a highly textured film formed with a preferred orientation along the [001] direction, and the analysis of the line-cut profile yielded a 23.1° angular distribution. These results indicated that for films deposited at higher T_d (0 °C), a more relaxed structure was formed, along with the formation of possible nanocrystals in the as-deposited amorphous film. Finally, a more detailed understanding of crystallization kinetics was obtained using a level-set simulation that employs the experimental parameters derived from x-ray measurements. The interfacial velocity and nucleation density were calculated for the textured microstructures, and the activation energy associated with growth was calculated as well. It was also shown that nanocrystalline domains form during deposition, and thus site-saturation nucleation took place in the films.

ACKNOWLEDGMENTS

This research was supported by the Northwestern University MRSEC (Grant No. NSF DMR-1121262). GIWAXS was performed at the APS DND-CAT 5BM-C station, which is supported through E. I. DuPont de Nemours & Co., Northwestern University (NU), The Dow Chemical Co., and the NSF funded MRSEC at NU. The authors thank Dr. Christian M. Schlepütz for assisting with the pole figure measurement at 33BM-C at APS. Use of the APS was supported by DOE-BES (Grant No. DE-AC02-06CH11357).

[1] A. Facchetti and T. Marks, *Transparent Electronics: From Synthesis to Applications* (John Wiley & Sons, Chichester, UK, 2010).

[2] D. S. Ginley and C. Bright, Transparent conducting oxides, MRS Bull. **25**, 15 (2000).

[3] E. Fortunato, P. Barquinha, and R. Martins, Oxide semiconductor thin-film transistors: A review of recent advances, Adv. Mater. **24**, 2945 (2012).

[4] S. Lee, S. Jeon, R. Chaji, and A. Nathan, Transparent semiconducting oxide technology for touch free interactive flexible displays, Proc. IEEE **103**, 644 (2015).

[5] J. F. Wager, B. Yeh, R. L. Hoffman, and D. A. Keszler, An amorphous oxide semiconductor thin-film transistor route to oxide electronics, Curr. Opin. Solid State Mater. Sci. **18**, 53 (2014).

[6] M. Lorenz, M. R. Rao, T. Venkatesan, E. Fortunato, P. Barquinha, R. Branquinho, D. Salgueiro, R. Martins, E. Carlos, and A. Liu, The 2016 oxide electronic materials and oxide interfaces roadmap, J. Phys. D **49**, 433001 (2016).

[7] T. Kamiya and H. Hosono, Material characteristics and applications of transparent amorphous oxide semiconductors, NPG Asia Mater. **2**, 15 (2010).

[8] K. Banger, Y. Yamashita, K. Mori, R. Peterson, T. Leedham, J. Rickard, and H. Sirringhaus, Low-temperature, high-performance solution-processed metal oxide thin-film transistors formed by a 'sol–gel on chip' process, Nat. Mater. **10**, 45 (2011).

[9] Y. H. Hwang, J.-S. Seo, J. M. Yun, H. Park, S. Yang, S.-H. K. Park, and B.-S. Bae, An 'aqueous route'for the fabrication of low-temperature-processable oxide flexible transparent thin-film transistors on plastic substrates, NPG Asia Mater. **5**, e45 (2013).

[10] Y. Kumaresan, Y. Pak, N. Lim, M.-J. Park, S.-M. Yoon, H.-M. Youn, H. Lee, B. H. Lee, and G. Y. Jung, Highly bendable In-Ga-ZnO thin film transistors by using a thermally stable organic dielectric layer, Sci. Rep. **6**, 37764 (2016).

[11] K. Nomura, H. Ohta, A. Takagi, T. Kamiya, M. Hirano, and H. Hosono, Room-temperature fabrication of transparent flexible

thin-film transistors using amorphous oxide semiconductors, Nature (London) **432**, 488 (2004).

[12] J. W. Hennek, J. Smith, A. Yan, M. G. Kim, W. Zhao, V. P. Dravid, A. Facchetti, and T. J. Marks, Oxygen "getter" effects on microstructure and carrier transport in low temperature combustion-processed a-InXZnO (X = Ga, Sc, Y, La) transistors, J. Am. Chem. Soc. **135**, 10729 (2013).

[13] J. Smith, L. Zeng, R. Khanal, K. Stallings, A. Facchetti, J. E. Medvedeva, M. J. Bedzyk, and T. J. Marks, Cation size effects on the electronic and structural properties of solution-processed In–X–O thin films, Adv. Electron. Mater. **1**, 1500146 (2015).

[14] X. Yu, T. J. Marks, and A. Facchetti, Metal oxides for optoelectronic applications, Nat. Mater. **15**, 383 (2016).

[15] W. Huang, L. Zeng, X. Yu, P. Guo, B. Wang, Q. Ma, R. P. Chang, J. Yu, M. J. Bedzyk, and T. J. Marks, Metal oxide transistors via polyethylenimine doping of the channel layer: Interplay of doping, microstructure, and charge transport, Adv. Funct. Mater. **26**, 6179 (2016).

[16] X. Yu, L. Zeng, N. Zhou, P. Guo, F. Shi, D. B. Buchholz, Q. Ma, J. Yu, V. P. Dravid, and R. P. Chang, Ultra flexible, "invisible" thin-film transistors enabled by amorphous metal oxide/polymer channel layer blends, Adv. Mater. **27**, 2390 (2015).

[17] T. Kamiya, K. Nomura, and H. Hosono, Present status of amorphous In–Ga–Zn–O thin-film transistors, Sci. Technol. Adv. Mater. **11**, 044305 (2010).

[18] A. P. P. Correia, P. M. C. Barquinha, and J. C. da Palma Goes, *A Second-Order* $\Sigma\Delta$ *ADC Using Sputtered IGZO TFTs* (Springer, Cham, Heidelberg, 2015).

[19] G. Liu, A. Liu, H. Zhu, B. Shin, E. Fortunato, R. Martins, Y. Wang, and F. Shan, Low-temperature, nontoxic water-induced metal-oxide thin films and their application in thin-film transistors, Adv. Funct. Mater. **25**, 2564 (2015).

[20] A. Klein, Transparent conducting oxides: Electronic structure-property relationship from photoelectron spectroscopy with in situ sample preparation, J. Am. Ceram. Soc. **96**, 331 (2013).

[21] R. Khanal, D. B. Buchholz, R. P. Chang, and J. E. Medvedeva, Composition-dependent structural and transport properties of amorphous transparent conducting oxides, Phys. Rev. B **91**, 205203 (2015).

[22] J. E. Medvedeva, D. B. Buchholz, and R. P. Chang, Recent advances in understanding the structure and properties of amorphous oxide semiconductors, Adv. Electron. Mater. **3**, 1700082 (2017).

[23] S. L. Moffitt, Q. Zhu, Q. Ma, A. F. Falduto, D. B. Buchholz, R. P. H. Chang, T. O. Mason, J. E. Medvedeva, T. J. Marks, and M. J. Bedzyk, Probing the unique role of gallium in amorphous oxide semiconductors through structure–property relationships, Adv. Electron. Mater. **3**, 1700189 (2017).

[24] D. C. Paine, T. Whitson, D. Janiac, R. Beresford, C. O. Yang, and B. Lewis, A study of low temperature crystallization of amorphous thin film indium-tin-oxide, J. Appl. Phys. **85**, 8445 (1999).

[25] D. E. Proffit, T. Philippe, J. D. Emery, Q. Ma, B. D. Buchholz, P. W. Voorhees, M. J. Bedzyk, R. P. H. Chang, and T. O. Mason, Thermal stability of amorphous Zn-In-Sn-O films, J. Electroceram. **34**, 167 (2014).

[26] M. Quaas, H. Steffen, R. Hippler, and H. Wulff, Investigation of diffusion and crystallization processes in thin ITO films by temperature and time resolved grazing incidence X-ray diffractometry, Surf. Sci. **540**, 337 (2003).

[27] P. K. Song, H. Akao, M. Kamei, Y. Shigesato, and I. Yasui, Preparation and crystallization of tin-doped and undoped amorphous indium oxide films deposited by sputtering, Jpn. J. Appl. Phys. **38**, 5224 (1999).

[28] F. O. Adurodija, L. Semple, and R. Brüning, Crystallization process and electro-optical properties of In_2O_3 and ITO thin films, J. Mater. Sci. **41**, 7096 (2006).

[29] S. Muranaka, Crystallization of amorphous In_2O_3 films during film growth, Jpn. J. Appl. Phys. **30**, L2062 (1991).

[30] D. B. Buchholz, Q. Ma, D. Alducin, A. Ponce, M. Jose-Yacaman, R. Khanal, J. E. Medvedeva, and R. P. Chang, The structure and properties of amorphous indium oxide, Chem. Mater. **26**, 5401 (2014).

[31] D. B. Buchholz, L. Zeng, M. J. Bedzyk, and R. P. Chang, Differences between amorphous indium oxide thin films, Prog. Nat. Sci.: Mater. Int. **23**, 475 (2013).

[32] G. González, J. Okasinski, D. Buchholz, J. Boesso, J. Almer, L. Zeng, M. Bedzyk, and R. Chang, Relationship between electrical properties and crystallization of indium oxide thin films using ex-situ grazing-incidence wide-angle x-ray scattering, J. Appl. Phys. **121**, 205306 (2017).

[33] M. Avrami, Kinetics of phase change I - General theory, J. Chem. Phys. **7**, 1103 (1939).

[34] M. Avrami, Granulation, phase change, and microstructure - Kinetics of phase change. III, J. Chem. Phys. **9**, 177 (1941).

[35] E. Pang, N. Vo, T. Philippe, and P. Voorhees, Modeling interface-controlled phase transformation kinetics in thin films, J. Appl. Phys. **117**, 175304 (2015).

[36] M. Moghadam and P. Voorhees, Thin film phase transformation kinetics: From theory to experiment, Scr. Mater. **124**, 164 (2016).

[37] J. Ilavsky, Nika: Software for two-dimensional data reduction, J. Appl. Crystallogr. **45**, 324 (2012).

[38] W. Ruland, X-ray determination of crystallinity and diffuse disorder scattering, Acta Crystallogr. **14**, 1180 (1961).

[39] L. E. Alexander, *X-ray Diffraction Methods in Polymer Science* (Wiley, New York, 1969).

[40] See Supplemental Material at http://link.aps.org/supplemental/10.1103/PhysRevMaterials.2.053401 for (1) the degree of crystallinity calculations (2) domain-size calculation, (3) the crystalline structure of indium oxide, (4) simulated x-ray diffraction pattern of bixbyite indium oxide, (5) all GIWAXS patterns, (6) a nontextured polycrystalline pole figure, and (7) electron microscopy images.

[41] B. D. Cullity and S. R. Stock, *Elements of X-ray Diffraction* (Prentice-Hall, Upper Saddle River, NJ, 2001).

[42] C. Mocuta, M.-I. Richard, J. Fouet, S. Stanescu, A. Barbier, C. Guichet, O. Thomas, S. Hustache, A. V. Zozulya, and D. Thiaudiere, Fast pole figure acquisition using area detectors at the DiffAbs beamline - Synchrotron SOLEIL, J. Appl. Crystallogr. **46**, 1842 (2013).

[43] D. Kriegner, E. Wintersberger, and J. Stangl, Xrayutilities: A versatile tool for reciprocal space conversion of scattering data recorded with linear and area detectors, J. Appl. Crystallogr. **46**, 1162 (2013).

[44] S. Osher and R. Fedkiw, *Level Set Methods and Dynamic Implicit Surfaces* (Springer Science & Business Media, Berlin, 2006).

[45] J. A. Sethian, *Level Set Methods and Fast Marching Methods: Evolving Interfaces in Computational Geometry, Fluid*

Mechanics, Computer Vision, and Materials Science (Cambridge University Press, Cambridge, England, 1999).

[46] C. Ganpule, A. Roytburd, V. Nagarajan, B. Hill, S. Ogale, E. Williams, R. Ramesh, and J. Scott, Polarization relaxation kinetics and 180 domain wall dynamics in ferroelectric thin films, Phys. Rev. B **65**, 014101 (2001).

[47] M. Moghadam, E. Pang, T. Philippe, and P. Voorhees, Simulation of phase transformation kinetics in thin films under a constant nucleation rate, Thin Solid Films **612**, 437 (2016).

[48] M. M. Moghadam, R. Li, D. B. Buchholz, Q. Li, P. W. Voorhees, and V. P. Dravid, In situ crystallization and morphological evolution in multicomponent indium oxide thin films, Cryst. Growth Des. **17**, 1396 (2017).

[49] M. M. Moghadam and P. W. Voorhees, Level-set simulation of anisotropic phase transformations via faceted growth, Comput. Mater. Sci. **143**, 454 (2018).

[50] G. Russo and P. Smereka, A level-set method for the evolution of faceted crystals, SIAM J. Sci. Comput. **21**, 2073 (2000).

[51] A. Walsh and C. R. A. Catlow, Structure, stability and work functions of the low index surfaces of pure indium oxide and Sn-doped indium oxide (ITO) from density functional theory, J. Mater. Chem. **20**, 10438 (2010).